Applied Mathematical Modelling 124 (2023) 713–733

Contents lists available at ScienceDirect

Applied Mathematical Modelling

journal homepage: www.elsevier.com/locate/apm

Formability prediction of interstitial-free steel via miniaturized tensile specimen for Rapid Alloy Prototyping

Lintao Zhang *, Will Harrison, Talal Abdullah, Shahin Mehraban, Nicholas P. Lavery

Future Manufacturing Research Institute, College of Engineering, Swansea University, Bay Campus, Fabian Way, Swansea SA1 8EN, UK

ARTICLE INFO

Keywords:
Steel development
Rapid alloy prototyping
Cross-die deep drawing
Interstitial-free steel
Forming limit diagram

ABSTRACT

This study aims to investigate the feasibility of using non-standard miniaturized tensile specimens (MTS) to characterize the formability features of interstitial-free (IF) steel, specifically DX57 steel. The motivation behind this research is to gain insight into the accuracy of predicted values for the steel's formability using the designed non-standard MTS, which could potentially be used to test materials obtained from rapid alloy prototyping (RAP) routines. Tensile tests were conducted using both standard bars and non-standard MTS with different angles to the rolling directions (0^o, 45^o, and 90^o) and the experiment results were used to determine the material properties for the following numerical simulations, which were based on the cross-die deep drawing concept. The results show that the non-standard MTS over-predicted the strain hardening exponent compared to the values obtained from the standard tensile bars. For the same punch stroke, the non-standard miniatured tensile specimen under-predicted the punch force. However, for the deformed blank, the thickness variation along different paths was compared, and the maximum thickness value difference was found to be less than 5%. In terms of the forming limit diagram (FLD), the MTS's prediction is very close to the standard test-piece's prediction; the overall major-minor strain status of the deformed blank is similar. The results of this research provide confidence in the ability to evaluate formability from small-scale tensile tests for heterogeneous alloys such as synthetic IF steels developed during RAP.

1. Introduction

Rapid Alloy Prototyping (RAP) is a process for quickly creating a synthetic alloy of two or more elements using minimal amounts of material. [1]. Compared to traditional methods, such as vacuum induction melt (VIM), RAP offers clear advantages. Its small scale of materials (20-40 g versus 25-60 kg for VIM [2]) allows for faster experimentation, making it critical for laboratory scale development. As a result, a goal of producing and testing 100 compositions per week has been set.

RAP is also used to investigate the effects of minor composition changes, such as evaluating the effects of residual elements in Interstitial Free (IF) steels. IF steel is a type of steel that is free of interstitial elements such as carbon, nitrogen, and oxygen. This steel has a low carbon content and is primarily used in applications that require deep drawing and forming. Therefore, formability is a key feature that needs to be investigated based on the application of IF steel. Sheet-metal forming involves two main groups of processes: cutting and plastic deformation. The latter group involves partial or complete plastic deformation of the work material. Deep drawing is a sheet metal forming process in which a sheet metal blank is drawn radially into a cylindrical or box-shaped

* Corresponding author.
E-mail address: L.Zhang@Swansea.ac.uk (L. Zhang).

https://doi.org/10.1016/j.apm.2023.08.022
Received 19 May 2023; Received in revised form 8 August 2023; Accepted 14 August 2023

Available online 21 August 2023

Table 1
Recent research related with cross-die deep drawing. BEL: blank edge length, BT: blank thickness, BHF: blank holder force. Exp. and N.S. denote experiment and numerical simulation, respectively.

Lead author	Year	Exp./N.S.	Alloy/Steel	BEL (mm)	BT (mm)	BHF (kN)	Friction coeff.
Atzema [3]	2004	Exp.& N.S.	DC04	230-330	0.7	150-330	0.13
Lingbeek [4]	2008	N.S.	-	-	-	-	0.1
Banabic [5]	2010	Exp.& N.S.	DC04	330	0.79 & 1	-	0.05
Banabic [5]	2010	Exp.& N.S.	Ac121-T4	260	1	-	0.05
Niazi [6]	2012	Exp.& N.S.	DP600	270	1	116.5	0.06
Ramazani [7]	2012	Exp.& N.S.	DP600	270	1	-	0.06
Kriechenbauer [8]	2015	Exp.& N.S.	Stainless steel	340 × 300	1	-	0.1
Deng [9]	2017	Exp.& N.S.	AA2016	260-300	1.7	< 1000	-
Habibi [10]	2018	Exp.& N.S.	TRIP700	270	1.2	667	0.05
Habibi [11]	2018	Exp.& N.S.	DP600	270	1	483	0.05
Muller [12]	2018	Exp.	DC01	280 × 320	0.9	50-100	-
Nakwattanaset [13]	2020	Exp.& N.S.	DP440	134	1.2	41.5	0.175
Kriechenbauer [14]	2021	Exp.& N.S.	DC01	320×360	1.16	50-500	0.13

forming die by the mechanical action of a punch. The drawability (limiting draw ratio: the ratio of the initial blank diameter to the diameter of the cup drawn from the blank) can be determined using this process. To better represent actual sheet forming processes, a cross-shaped die was developed in addition to round and square dies. Compared to round or square cups, the cross-shaped die possesses many different forming modes, making it a better representation of actual sheet forming processes.

The Cross-Die test was initially developed as part of the Brite-Euram Light Weight Vehicle project [3]. In a study by Lingbeek et al. on the tool and blank interaction in the cross-die forming process [4], it was found that the accuracy of the modelling results heavily depends on the contact algorithm parameters. Softer penalty factors, set at 0.1 times the default penalty contact stiffness, can reduce numerical issues and computational time while providing a more uniform pressure on the deformed blank. Banabic investigated the influence of different yield surface models (Hill 1948, BBC 2005-4, BBC 2005-6, and BBC 2005-7) on the thickness distribution along various paths in their study [5]. The results indicated that the BBC 2005-7 model was sufficiently accurate for DC04 and Ac121-T4 alloys. In a separate study, Niazi et al. investigated failure predictions for dual-phase steel using anisotropic damage [6]. They found that the model without damage was unable to predict the actual punch stroke that could cause blank damage. However, simulations with modified isotropic and anisotropic damage models were able to predict failure at the actual punch depth and location observed in the experiments. However, anisotropic damage models are considered to be more accurate. Ramazani et al. studied the failure process of DP600 steel using the cross-die test and identified the parameters required for the Gurson-Tvergaard-Needleman (GTN) model using response surface methodology (RSM). The modelling results were found to be in agreement with the experimental predictions [7]. Kriechenbauer et al. compared the thickness distribution of the deformed blank between cases with and without bi-directional deep drawing (BDD), a variant of cross-die deep drawing. The results indicated that increasing the transferable drawing forces over the weak point at the punch radius is a valid approach, as shown by Kriechenbauer et al. [8]. In another study by Deng and Hennig [9], the influence of different strain hardening models (Swift, Ghosh, Hockett-Sherby, and Combined S/H-S) on the deformed blank results was investigated. Habibi et al. [10] conducted studies on the failure mechanisms of TRIP700 steel sheets and DP600 steel sheets, respectively [11]. For TRIP700 steel, three damage models were employed: the Tresca, Situ, and Martinez-Donaire models. The Tresca model could calculate the damage initiation if shear failure was dominant, while the Situ model predicted accurately when localized necking was dominant. Regarding the DP600 steel, various fracture criteria were utilized, including the Maximum Shear Stress, Oh, Johnson–Cook, Modified Mohr-Coloumb, and Lou and Huh criteria, respectively, to determine the fracture strain values. However, the equivalent strains at fracture were calculated differently by each model. Muller et al. analyzed the elastic boundary conditions of press machines for modelling the deep-drawing process. The results showed that the measured distances between the inner and outer surfaces varied around the initial sheet thickness, confirming the quality of the measurement method [12]. Nakwattanaset et al. determined the strain- and stress-based forming limit curves of DP440 steel sheet: Both FLSCs were noticeably dissimilar, especially in a fairly-wide range of loading directions from plane strain to biaxial stress, and thus allegedly affected by the choice of applied yield criteria [13]. Kriechenbauer et al. studied the evolutionary optimization of deep-drawing processes on servo screw presses and the results indicated that the method is a suitable tool for the development of deep drawing processes with superimposed low-frequency vibrations on a servo screw press [14]. Table 1 showed the recent research related with cross-die deep drawing. In this work, the cross-shape die was used to conduct deep drawing on the objective material.

As previously discussed, one limitation of the RAP process is its inability to provide large amounts of material. The materials are not enough either for the Nakajima test, which is employed to obtain forming limit curves by typically using circular sheet metal specimens with a diameter of > 200 mm, or for the Erichsen dome is used to evaluate the stretch-forming of sheet metals. The materials are also not enough to extract standard tensile specimens, such as the ISO/EN A80, from strips manufactured using this process. Consequently, non-standard miniaturized tensile specimens (MTS) must be used. Zhang et al. conducted tensile tests on various dimensions of these MTS to correlate the mechanical properties, such as yield strength and ultimate tensile strength, with different types of steel: Dual-Phase steel and 316L stainless steel [15], DP800 steel [16] and IF steel [17]. However, it is unclear how using sub-sized tensile specimens affects formability measurements for certain steels, such as IF steel (e.g., DX57), as no documentation on this topic has been found.

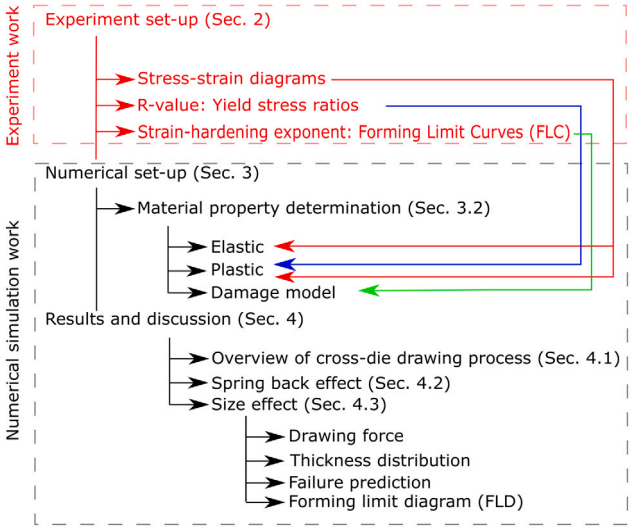

Fig. 1. Storyline of this work. Experiment results are used to determine the material properties of DX57 steel, which are used for the following numerical simulations.

The main objective of this work is to establish a correlation between the formability predictions of standard and non-standard bars and further investigate the suitability of miniaturized tensile specimens (MTS) for predicting the formability of DX57 steel. The research involves both experimental work and numerical simulation and the main storyline of the current work as illustrated in Fig. 1 (The Sections of Introduction and Conclusions are not shown).

2. Experimental methodology and results

2.1. Material

DX57 steel was chosen for the experiment due to its wide application and typical microstructure, as shown in Fig. 2 (a). The microstructure of IF steel is typically composed of ferrite grains with small amounts of other phases such as pearlite and bainite. The grain size of the ferrite is typically small and uniform due to the low carbon content and the addition of elements such as titanium and niobium that promote grain refinement.

2.2. Experiment set-up and procedure

Five groups of tensile test pieces with different dimensions were manufactured: A80 (gauge length = 80 mm), A50 (50 mm), ASTM25 (25 mm), Mini1 (10 mm), and Mini2 (5 mm), respectively. The dimensions of A80 and A50 conform to ISO 6892-1 standard [18], and ASTM25 conforms to ASTM E8/E8M-13a standard [19]. Mini1 and Mini2 are non-standard tensile bars, which were potentially used for limited material development by the RAP process. The detailed dimensions of these five groups have been previously described. All test pieces have the same thickness, 0.8 mm, as they were manufactured from the same strip. A80, A50, ASTM25, and Mini1 test pieces were made through computer numerical control (CNC) machining, and Mini2 test pieces were manufactured using electrical discharge machining (EDM) methods to minimize deformation prior to testing. To determine the r-value of DX57, bars with longitudinal (0^o), diagonal (45^o), and transverse (90^o) orientations to the rolling direction were made for each group/dimension of test pieces. The Tinius Olsen H25KS tensile machine and the video extensometer (XSight 9MPX) were used to capture stress and strain during the tests. The test procedure followed the standard of BS/EN/ISO6892-1:2009 [18]. The tensile bar and experimental setup are shown in Fig. 2 (b) and (c).

2.3. Experiment results

2.3.1. R-values and yield stress ratio

The normal anisotropy is measured by the plastic strain ratio (R-value), which is defined as the ratio of the width strain to the thickness strain. It can be calculated using the following equation:

$$R = \frac{\ln(w_0/w)}{\ln(h_0/h)}, \tag{1}$$

where w_0 and w denote the initial and final width, and h_0 and h denote the initial and final thickness. Table 2 shows the R-values of DX57 for different sizes of test-pieces whilst the strain equals 20%. The discussion about the trends is not the focus of this work, as they were extensively discussed in a separate publication [17]. In this study, R-values are used to calculate yield stress ratios (R_{ij})

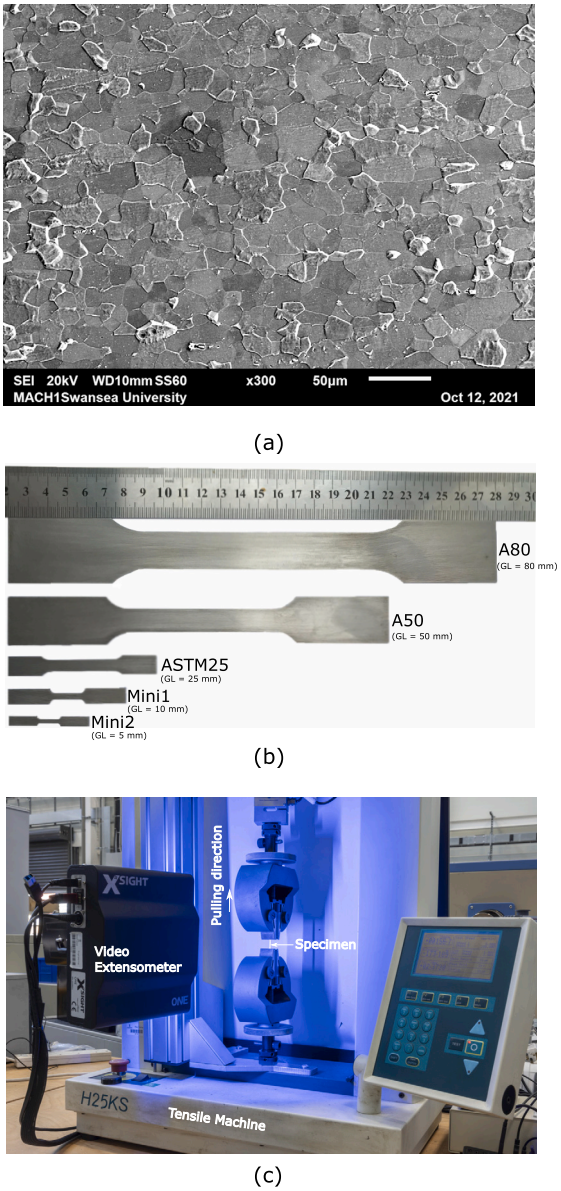

Fig. 2. (a) Typical microstructure of DX57. The maximum chemical compositions (weight percentage) of C, Si, Mn, P, S and Ti for DX57 are 0.12%, 0.5%, 0.6%, 0.1%, 0.036% and 0.3%, respectively. (b) The adopted tensile bars. The gauge length (GL) values for A80, A50, ASTM25, Mini1 and Mini2 are 80, 50, 25, 10, and 5 mm, respectively. All the bars have a identical thickness 0.8 mm. (c) The adopted tensile machine (H25KS) and video extensometer (Xsight ONE).

Table 2
The R-values of DX57 for different size of bars. 0^o, 45^o and 90^o stand for the angle between the tension direction and the rolling direction of the strip.

	A80	A50	ASTM25	Mini1	Mini2
0^o	1.99	2.00	2.01	2.27	2.1
45^o	1.75	1.81	2.01	2.22	1.97
90^o	2.74	2.49	2.57	2.73	2.37

using the Hill48 model, in order to define the yield behaviour of DX57. For a thin plate, the R_{ij} values can be calculated using the following equations:

$$R_{11} = R_{13} = R_{23} = 1, \tag{2}$$

Table 3
The yield stress ratio values of DX57 for different size of bars ($R_{11} = R_{13} = R_{23} = 1$).

	A80	A50	ASTM25	Mini1	Mini2
R_{22}	0.63	0.66	0.65	0.62	0.66
R_{33}	0.68	0.71	0.7	0.62	0.66
R_{12}	1.39	1.44	1.49	1.51	1.50

Table 4
Strain hardening exponent n for different size of bars. Non-standard test pieces give higher n values ($\sim$ 18.5%) compared to standard ones.

	A80	A50	ASTM25	Mini1	Mini2
Test1	0.211	0.225	0.225	0.271	0.280
Test2	0.209	0.203	0.221	0.259	0.293
Test3	0.219	0.242	0.229	0.258	0.235
Mean	0.213	0.224	0.225	0.263	0.269

$$R_{22} = \frac{1}{\sqrt{\frac{r_0}{r_{90}(1+r_0)} + \frac{r_0}{(1+r_0)}}}, \tag{3}$$

$$R_{33} = \frac{1}{\sqrt{\frac{r_0}{r_{90}(1+r_0)} + \frac{1}{(1+r_0)}}}, \tag{4}$$

and

$$R_{12} = \sqrt{\frac{3(r_0+1)r_{90}}{(2r_{45}+1)(r_0+r_{90})}}, \tag{5}$$

where r_0, r_{45} and r_{90} denote the R-values 0, 45 and 90 degrees to the rolling direction. The subscripts 1, 2, and 3 of R stand for the rolling direction (RD), transverse direction (TD) and thickness direction, respectively. Table 3 shows the yield stress ratio values of DX57 for different size of bars.

2.3.2. Strain-hardening exponent and forming limit curve

The strain hardening exponent n is determined by using Hollomon strain-hardening equation [20]:

$$\sigma = k\epsilon_p^n, \tag{6}$$

where, k is the strength coefficient, defined as the true strength at a true strain of 1. Table 4 displays the n values, along with their three repeats, for different sizes of tensile bars. The results revealed that the n-values predicted by the standard bars were in the range of 0.2 to 0.24, which is consistent with Ferreira et al.'s work where $n = 0.24$ was reported for a longitudinal test-piece [21]. On the other hand, the n-values predicted by the non-standard bars were in the range of 0.24 to 0.29, indicating higher predictions than the standard bars. Generally, smaller bar sizes will have higher n-values than larger bar sizes for a given material. This is because smaller bars are subject to higher levels of plastic deformation and are more likely to experience necking, which increases strain hardening. That can also be understood as follows: This is because the larger bar sizes result in a more uniform deformation across the specimen, which can limit the amount of strain hardening that occurs. In contrast, smaller bar sizes result in more localized deformation, which can lead to greater strain hardening. On average, the difference percentage between the two sets of predictions is around 18.5%. The averaged n-values were used to determine the forming limit curves.

In this work, Keeler-Brazier formula was used to determine the forming limit curves [22]:

$$\epsilon_1 = \begin{cases} FLD_0 + \epsilon_2(0.784854 - 0.008565 \times \epsilon_2) & \epsilon_2 \le 0, \\ FLD_0 + \epsilon_2(0.027254 \times \epsilon_2 - 1.1965) & \epsilon_2 > 0, \end{cases} \tag{7}$$

where FLD_0 is:

$$FLD_0 = \frac{n}{0.2116}(23.25 + 356.1 \times C_1), \tag{8}$$

where C_1 is:

$$C_1 = \begin{cases} t & t \le 0.0118, \\ 0.0118 & t > 0.0118, \end{cases} \tag{9}$$

where ϵ_1, ϵ_2, n and t stand for major strain, minor strain, strain hardening exponent and plate metal thickness, respectively. The forming limit curves were presented in Fig. 3. The non-standard test pieces yielded higher forming limit curves (FLC) than the

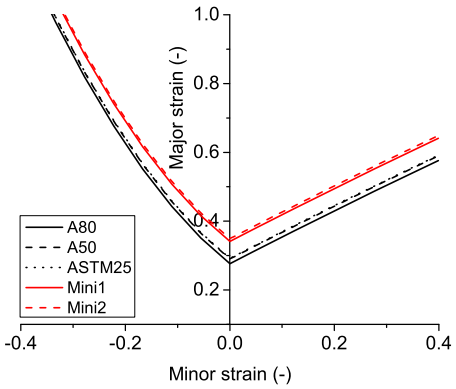

Fig. 3. Forming limit curves for different size of bars. Non-standard test pieces (in red) give higher FLC compared to the standard bars (in black) prediction.

standard bars, with the curves shifting upwards. This could be attributed to the higher n values obtained from the non-standard bars and which exhibits lower rates of work hardening.

3. Numerical simulation methodology

3.1. Geometry

The cross-die deep drawing system includes 4 parts: the punch, the blank holder, the die and the blank, respectively. A quarter of the system was adopted due to the symmetric feature as showed in Fig. 4 (a). The punch, blank holder and die were modelled as three dimensional (3D) rigid bodies whose motion was governed by the reference node and the blank were defined as 3D deformable shell: this setting has been validated in the previous work by Habibi et al. [10], Chen et al. [23] and Bouchaala et al. [24]. The dimensions of the blank, blank holder, punch, and die were determined based on previous research. The dimensions of the punch, blank holder, and die are shown in Fig. 4 (b), (c), and (d), respectively, according to Banabic's work [5]. For this study, a square blank with an edge length of 270 mm was selected, as shown in Fig. 4 (e). This size is widely used in previous studies, as shown in Table 1.

3.2. Numerical set-up

Five groups of numerical simulations were conducted using the experimental results based on 5 different test-piece dimensions: A80, A50, ASTM25, Mini1, and Mini2. These five groups of modelling results are named G-A80, G-A50, G-ASTM25, G-Mini1, and G-Mini2, respectively. The numerical set-up for each group is identical, but the material properties' values are different, as the experiments did not provide identical stress-strain diagrams for different sizes of the test-pieces.

The elastic and plastic properties of DX57 steel were determined through the uniaxial tensile test, and the experiment setup was discussed in Sec. 2. The density, Young's modulus and Poisson's ratio were found to be 7800 kg/m^3 210 GPa and 0.3, respectively, for all specimen dimensions. The plastic properties, represented by the proof stress vs. plastic strain curve, were determined from the engineering stress-strain curves, and the Johnson-Cook method was used to evaluate the true stress (σ_T) values after ultimate tensile strength point. It is worth noting that during the experiment, variations in results were observed among tensile specimens of different sizes for all the steel samples, indicating a size effect or scale dependency. These differences consequently lead to variations in plastic properties across different simulation sets. Utilizing the actual experimental results obtained from various sizes of tensile bars can present a worst-case scenario. If the results from this worst-case scenario are deemed acceptable, it will instill greater confidence in the feasibility of non-standard miniature tensile bar designs. The detailed relationship of proof stress and plastic strain as showed in Table 5.

The Abaqus/Explicit solver was adopted to simulate cross-die deep drawing process as it has been validated by the other work of Habibi et al. [10], Wu et al. [25], Robert et al. [26], Ayari et al. [27] and Wifi et al. [28]. Additionally, the spring back effect was also considered for all the simulations due to the results need to be compared at the 'steady-state'. Therefore, two steps were involved for each modelling case: the drawing and spring-back steps, both using Dynamic/Explicit solver.

According to previous research (Table 1), the friction coefficients between the blank and the punch, blank holder, and the die are in the range of 0.05-0.2. Therefore, in the current work, a friction coefficient of 0.15 is used. The blank holder force (BHF) varies widely depending on the steel used, as it affects the shape of the blank edges (wrinkled, fully drawn, or torn). In the current work, the BHF is determined using the following equations [29]:

$$F_{BH} = p \times A_{BH}, \tag{10}$$

where p and A_{BH} are blank holder pressure and area. Here:

$$p = [(\beta_a - 1)^2 + \frac{d}{200 \times s}] \times \frac{R_m}{400}, \tag{11}$$

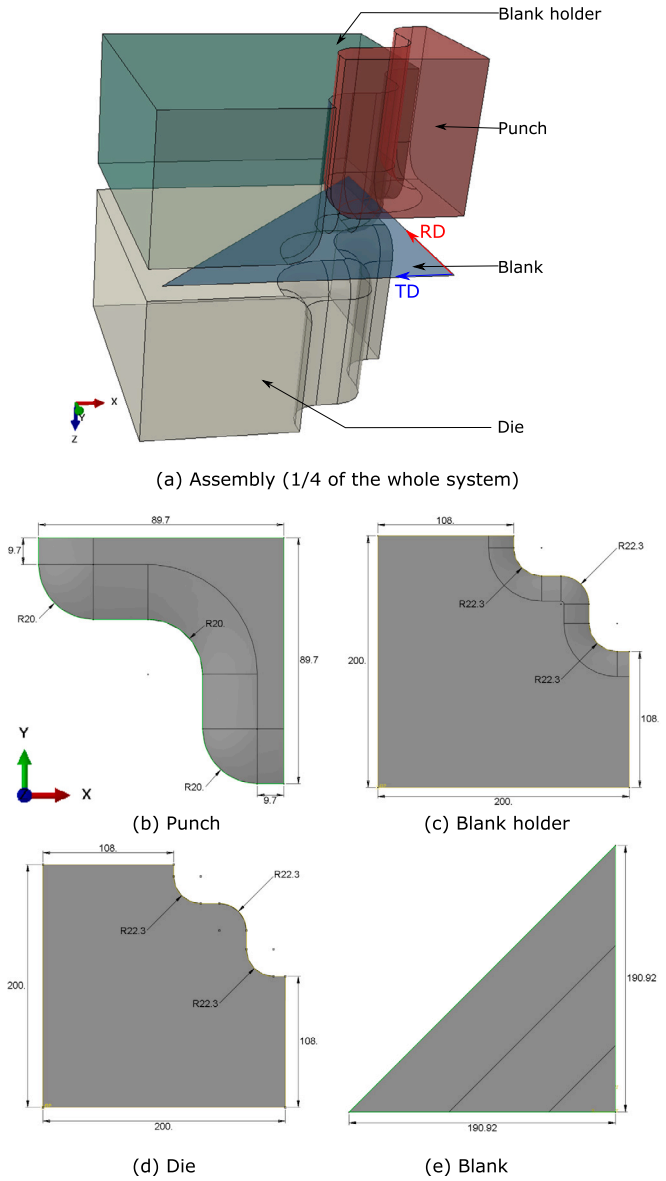

Fig. 4. (a) The assembly of the blank holder, the punch, the blank and the die. Only a quarter is showed due to symmetric feature. RD and TD denote the rolling and transversal directions. (c) - (d) have the same coordinate system as (b). The unit is in millimetre.

Table 5
The relationship of proof stress and plastic strain used for different numerical simulation groups.

G-A80		G-A50		G-ASTM25		G-Mini1		G-Mini2	
Proof stress (MPa)	Plastic strain (-)	Proof stress (MPa)	Plastic strain (-)	Proof stress (MPa)	Plastic strain (-)	Proof stress (MPa)	Plastic strain (-)	Proof stress (MPa)	Plastic strain (-)
30.0000	0.0000	30.0000	0.0000	30.0000	0.0000	30.0000	0.0000	30.0000	0.0000
91.6939	0.0005	88.3552	0.0005	78.8936	0.0005	53.9589	0.0005	50.1711	0.0005
106.2820	0.0010	103.1959	0.0010	92.2091	0.0010	64.7491	0.0010	60.4548	0.0010
123.1911	0.0020	120.5295	0.0020	107.7719	0.0020	77.6971	0.0020	72.8463	0.0020
149.7409	0.0050	147.9898	0.0050	132.4469	0.0050	98.8696	0.0050	93.2081	0.0050
173.5641	0.0100	172.8473	0.0100	154.8010	0.0100	118.6407	0.0100	112.3132	0.0100
201.1774	0.0200	201.8800	0.0200	180.9279	0.0200	142.3655	0.0200	135.3342	0.0200
244.5347	0.0500	247.8745	0.0500	222.3525	0.0500	181.1602	0.0500	173.1624	0.0500
283.4391	0.1000	289.5094	0.1000	259.8805	0.1000	217.3871	0.1000	208.6559	0.1000
328.5332	0.2000	338.1375	0.2000	303.7424	0.2000	260.8583	0.2000	251.4246	0.2000
399.3378	0.5000	415.1757	0.5000	373.2862	0.5000	331.9425	0.5000	321.7019	0.5000
429.0083	0.7000	447.6768	0.7000	402.6435	0.7000	362.6557	0.7000	352.1778	0.7000

where β_a, d, s and R_m represent the actual draw ratio, punch diameter, sheet thickness and tensile strength of the material, respectively. The blank holder area can be calculated through the following equation:

$$A_{BH} = (D^2 - d_e^2) \times \pi/4, \tag{12}$$

where D and d_e are diameter of the blank and the effective diameter of the blank holder. d_e can be defined by the following equation:

$$d_e = d + 2w + 2r_M, \tag{13}$$

where w and r_M are drawing clearance and die edge curvature radius. Based on the above equations, 7374 N was selected as the BHF for 1/4 system as showed in Fig. 4 (a). The symmetric boundary conditions were used for the blank edges. The die was fixed in both drawing and spring back processes. BHF was applied on the reference pointed, which is linked to the blank holder and the holder can move along the punch direction. The draw depth is 50 mm for the current work. For the spring-back step, the BHF was removed which allows the deformed blank to spring back. The linear quadrilateral elements of type S4R was selected for the blank. The total nodes and elements numbers are 1465 and 1395, respectively.

In the numerical simulation, The Forming Limit Diagram (FLD) damage initiation criterion was adopted. It is intended to predict the onset of necking instability in sheet metal forming. The FLD damage initiation criterion requires the specification of forming limit curve (FLC) in tabular form by giving the major principal strain at damage initiation as a tabular function of the minor principal strain. These data was obtained through the experiment (see Sec. 2.3.2). The damage variable, FLDCRT, was defined as the maximum value of the FLD damage initiation criterion ω_{FLD}:

$$\omega_{FLD} = \frac{\epsilon_{major}}{\epsilon_{major}^{FLD}(\epsilon_{minor}, \theta, f_i)}, \tag{14}$$

where ϵ_{major}, ϵ_{minor}, θ and f_i are the major principal strain, the minor principal strain, the temperature and the predefined field variables, respectively.

3.3. Machine learning and k-means clustering

K-means, one of the prototype-based clustering methods, is used to analysis the data of major and minor strains. The k-means method represents each cluster by its centre and iteratively updates the centre and data point assignments to the centres until convergence criteria are met. Specifically, let $X \in R^{n \times d}$ denote the n data points with d dimensions, $C \in R^{k \times d}$ the k centres, and S_j the membership set of the cluster j. The k-means randomly decide the initial centres first and repeats the following two steps until the centres do not change:

1. Assign each data point to the cluster S_j having the centre c_j that minimizes the mean-squared error distance (MSE distance).

$$argmin_{j \in (0,1,2 \ldots k)} ||x_i - c_j||^2 \tag{15}$$

2. Update the centres c_j by averaging the data points x_i in the cluster S_j.

$$c_j = \frac{1}{||S_j||} \sum_{x_i \in S_j} x_j \tag{16}$$

Another question is to determine the number of clusters. This is decided by the Silhouette scores. For a data point i, here:

$$s(i) = \frac{b(i) - a(i)}{\max\{a(i), b(i)\}}, \text{ if } |C_I| > 1 \tag{17}$$

and

$$s(i) = 0, \text{ if } |C_I| = 1, \tag{18}$$

where $s(i)$ is the silhouette score, $b(i)$ and $a(i)$ denote a measure of how dissimilar i is to its own cluster, and $|C_I|$ is the number of points belonging to cluster i. Thus an $s(i)$ close to 1 means that the data is appropriately clustered.

4. Results and discussion

4.1. Overview of cross-die deep drawing process

Similar to the Swift test (flat-bottom cylindrical cup), the deformed blank in cross-die deep drawing can also be divided into three regions: the flange, the cup wall, and the punch region, as shown in Fig. 5. Unlike in cup drawing, the strain distribution along the circumferential direction of the cup wall is not uniform, as shown in Fig. 5 (b). The reason for the formation of these four parts is due to the different stress states during the drawing process.

In the flange region, it is in contact with the blank holder and the die during drawing, resulting in a stress perpendicular to the blank. The outer circumference of the blank is decreased as the material is drawn to the die, resulting in compressive strain along the circumference and tensile strain along the radial direction, as shown in Fig. 6. It is also noted that the side and middle of the flange

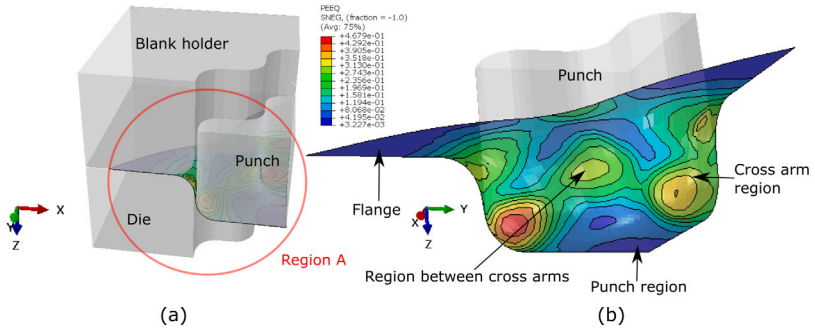

Fig. 5. (a) the simulation domain and (b) the enlargement of Region A. Four regions on the deformed blank: the flange, cup wall, the punch region and the region between cross arms. Results obtained from G-A80. The contour represents equivalent plastic strain (PEEQ) level.

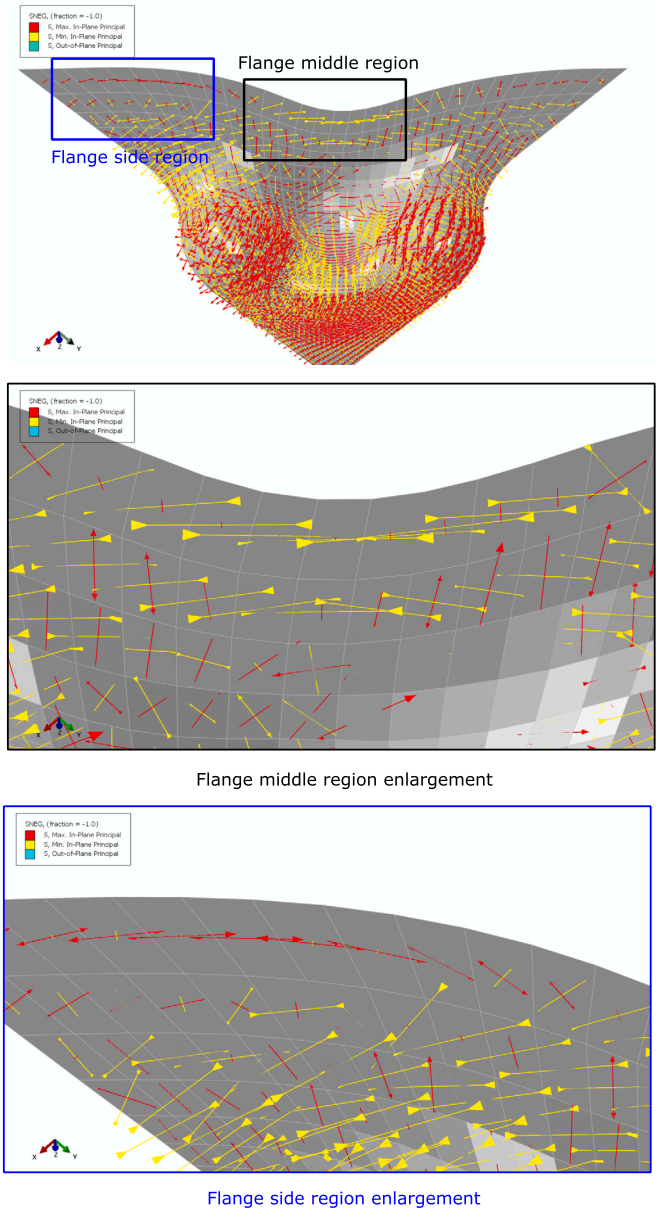

Fig. 6. Maximum and minimum Principal stress distribution on the deformed blank at the end of drawing: Flange region.

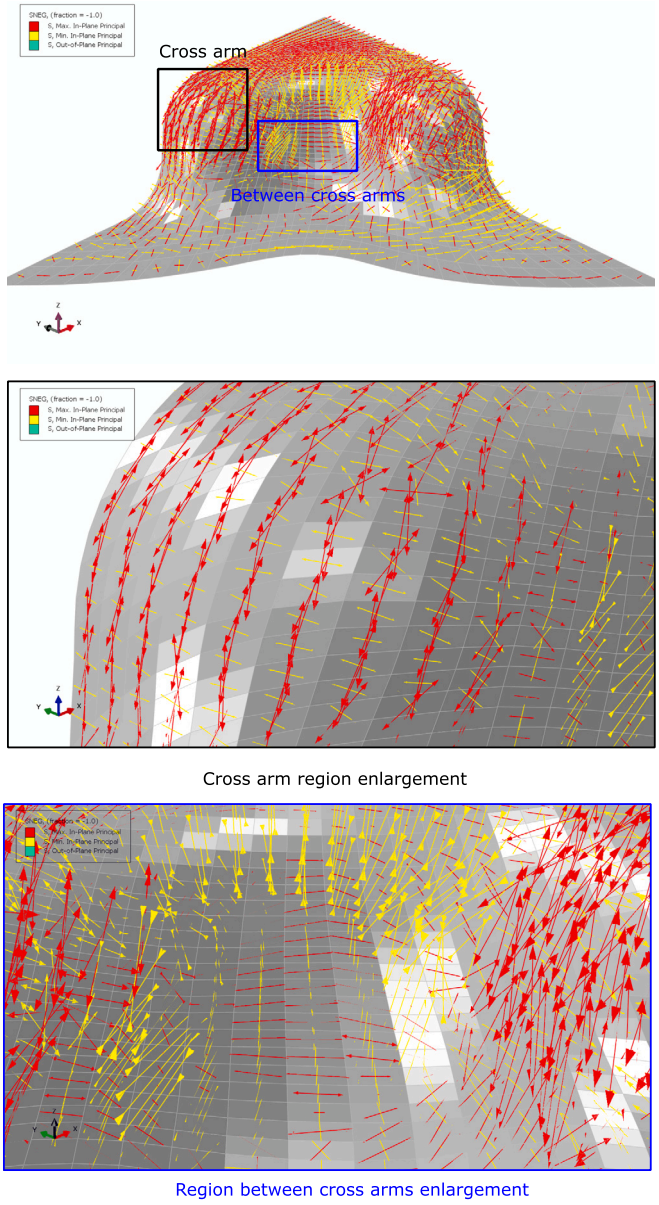

Fig. 7. Maximum and minimum Principal stress distribution on the deformed blank at the end of drawing: Cross punch arm ends and between arm regions.

undergo different behaviours: the side region undergoes mainly maximum principal stress which results in the thinning process, while the middle region mostly undergoes the minimum principal stress which will cause the thickness to increase. The quantitative discussion on the thickness variation will be conducted in Sec. 4.3.2. Fig. 7 showed the stress distribution for the cross arm region and the region between the cross arms. The results indicate that for the regions in contact with the cross arms, the maximum stress is dominant, compared to the minimum stress, which is similar to the cup deep drawing. That means the tensile deformation is dominant. This is easy to be understood, as the blank is deforming along this tensile direction. For the regions between the cross arms, it undergoes both maximum and minimum stress, however, the direction of them were changed. For the cross arm region, the maximum stress direction is the same as the drawing direction (along z-axis in this work) and the minimum stress is perpendicular to it. For the region between arms, the minimum stress direction is the same as x-axial and the maximum stress is perpendicular to it. This indicated that the blank in that region was stretched to the cross arm region. The failure may first occur at this region for some steels, dual-phase 600 steel for instance [7]. For the punch region (Fig. 8), a biaxial tensile stress is present due to the punch operation, as this part of the blank comes into contact with the cross-shaped punch head. The nature of this region is similar to the stress distribution in the cup bottom region during the Swift test. Compared to round cup deep drawing, cross-die deep drawing allows for the creation of more complex shapes and features and offers many different forming modes and deformation paths. This makes it a suitable method for studying the formability features of the target steel.

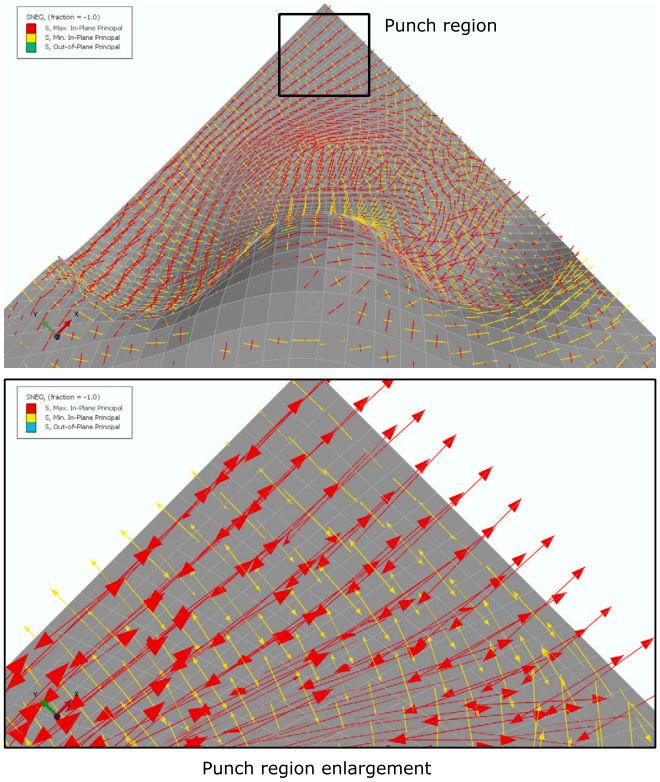

Fig. 8. Maximum and minimum Principal stress distribution on the deformed blank at the end of drawing: Punch region.

4.2. Spring-back effect

The spring-back effect is typically the result of the elastic properties of the deformed material, which causes it to return to its original shape when the forming tools are removed. This effect can impact the accuracy of the final part and is present in all forming operations. The amount of spring-back in deep drawing is influenced by several factors, such as the material properties of the metal, sheet thickness, and draw depth, as well as the die and punch design. To address spring-back, designers may employ overforming, which involves drawing the sheet metal deeper into the die than the final desired depth to compensate for the effect. However, this technique is not the primary focus of the current work. Springback has little effect on plastic strain or thickness, but will affect final displacement, hence it's important for forming specific shapes such as sheet metal packaging or automotive body panels.

Fig. 9 shows the contour comparison between the stress, the equivalent plastic strain (PEEQ), the blank thickness (STH) and the damage variable (FLDCRT) at the end of drawing (a), (c), (e) and (g) and spring-back (a), (c), (e) and (g). The results indicate that the spring-back effect has little influence on the strain, thickness, and damage parameter of DX57 steel with a thickness of 0.8 mm and a stroke of 50 mm. The change in stress distribution after the external forces are removed is not surprising, as it is an indication that the elastic strain has been released. This can be further supported by the fact that the ratio of the true stress to the Young's modulus is a measure of elastic strain.

4.3. Size effect

In this section, the focus is on the question of whether the designed MTS can predict the formability features of RAP materials. To compare the results, the benchmark results obtained from standard tensile bars. The size effect of the test piece on the forming force, thickness distribution, failure prediction, and forming limit diagrams were studied.

4.3.1. Forming force

Fig. 10 shows the punch force evolutions against the drawing time for different simulation groups cases. Firstly, during the drawing stage (0 - 0.75 s), the forces increase almost linearly for all cases. This is because the punch force is mainly used to balance the ideal force for blank deformation (which increases linearly) and the frictional forces during this period. Towards the end of the drawing stage (0.75 - 1 s), the force curve becomes flat. This is because the friction force decreases as the sheet metal is stretched and thinned, making it easier to deform and reducing the amount of friction between the deformed blank and the die. During the

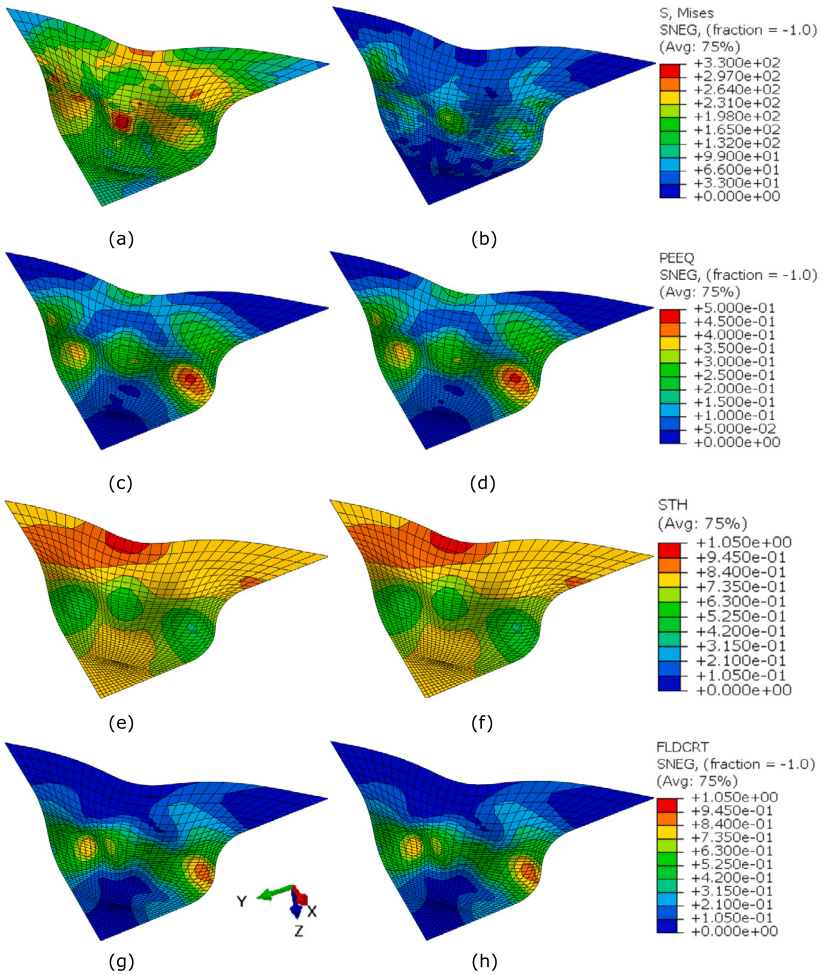

Fig. 9. The contour comparison between drawing and spring-back processes. (a) and (b): Stress, (c) and (d): Plastic strain, (e) and (f): Thickness and (g) and (h) damage variable. The spring-back process has effect on the stress status, however, has little effect on the plastic strain, the thickness and the damage parameter distribution. Results obtained from G-A80.

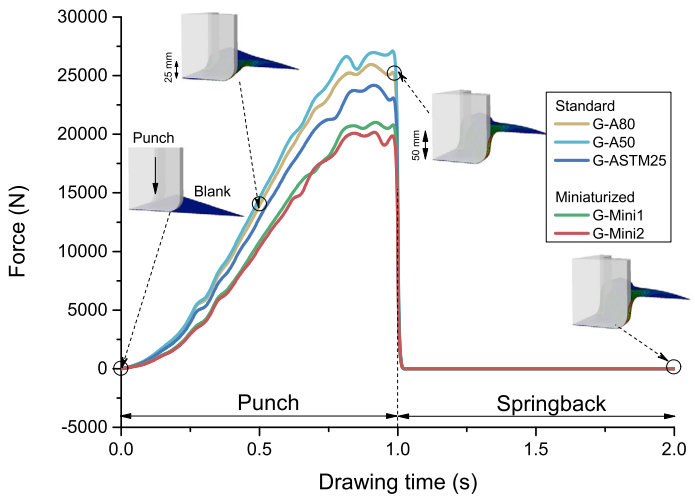

Fig. 10. Punch force evolutions against the drawing time for different simulation groups cases. Compared to standard, the miniaturized bars' results require a lower punch force.

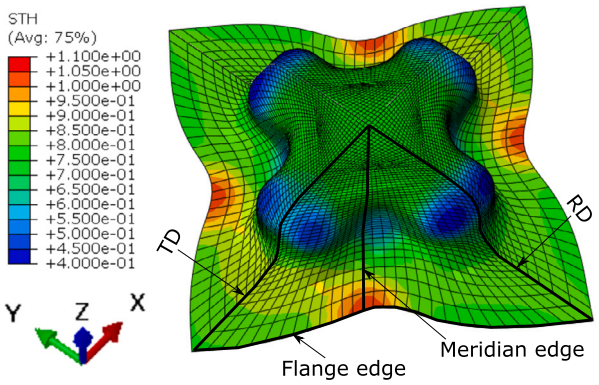

Fig. 11. The thickness (STH) contours on the deformed blank at the end of spring back (A80 case). Four paths were defined: flange edge, diagonal edge 1, diagonal 2 and meridian edge, respectively.

spring-back stage (1 - 2 s), the forces decrease to zero at 1 s, as the blank holder and punch forces are released. Furthermore, the maximum punch force for the cross-die deep drawing was compared an empirical equation used to predict the maximum punch force for the round cup drawing. The maximum drawing force P_{max} can be expressed as:

$$P_{max} = \frac{2}{\sqrt{3}} s_u \pi D_p h, \tag{19}$$

where s_u, D_p and h denote tensile strength of the material, the punch diameter and the blank thickness, respectively. For the cross shape punch, the equivalent punch diameter should be used. Therefore, here:

$$\begin{aligned} P_{max}^{cross} &= \frac{2}{\sqrt{3}} s_u \pi D_p h \\ &= \frac{2}{\sqrt{3}} [-] \times 300[N/mm^2] \times 3.14[-] \times 151.3[mm] \times 0.8[mm] \\ &= 131662.4N. \end{aligned} \tag{20}$$

Therefore a quarter of the whole system requires (∼) 33000 N. This value is in the same magnitude to the maximum drawing force predicted by our simulation, as showed in Fig. 10.

Secondly, when comparing the force curves between different cases, it was observed that the standard tensile test-pieces predicted a higher required punch force than the forces predicted by the non-standard test-pieces. The force difference between the standard and non-standard test-pieces was 20.7% at the end of the punching stage (1 s). This value was calculated using the averaged force values for the standard bars and the non-standard bars. These results indicate that the material predicted by using the non-standard test-piece shows a more ductile feature compared to that predicted by the standard test-piece. This is consistent with the determined strain hardening exponents: larger n for non-standard bars compared to standard bars.

4.3.2. Thickness distribution

The thickness distribution of a deep-drawn part can have a significant impact on its mechanical properties, as it varies in areas experiencing compressive versus tensile stresses. Fig. 11 illustrates the thickness distribution (STH) of the deformed blank for the G-A80 case at the end of the spring-back stage. The results show that the thickest regions of the deformed blank are located in the vicinity of the middle of the flange. This is due to the thickening effect during the drawing process. In this region, the minimum principle stress is dominant, and the material experiences compressive stresses. More material flows to this region. The thinnest regions are located in the vicinity of the ends of the cross arms, and there is another thinning region observed between the cross-shaped arms. These thinnest regions are the locations where potential failure can occur.

Four paths were defined: flange edge, TD, RD and meridian edge, respectively, to study the size effect. Fig. 12 shows the thickness (STH) contours on the deformed blank at the end of spring back for different cases. The results show that for all the paths, the thickness predicted by the non-standard bars is similar to that value predicted by the standard test-piece. The maximum thickness value difference is 2.3%, as showed in Fig. 12 (a) between G-Mini2 and G-A80 at distance of 111.8 mm.

4.3.3. Failure prediction

The occurrence of damage is typically observed at the thinnest point on the deformed blank, where the material experiences high tensile stresses and is stretched out. Typically, the thinner areas of the part will have reduced strength and may be more susceptible to deformation or failure. Fig. 13 illustrates the distribution of the damage variable (FLDCRT) value on each node of the deformed blank at the end of spring-back stage. The results indicate that some locations have already experienced damage with FLDCRT values

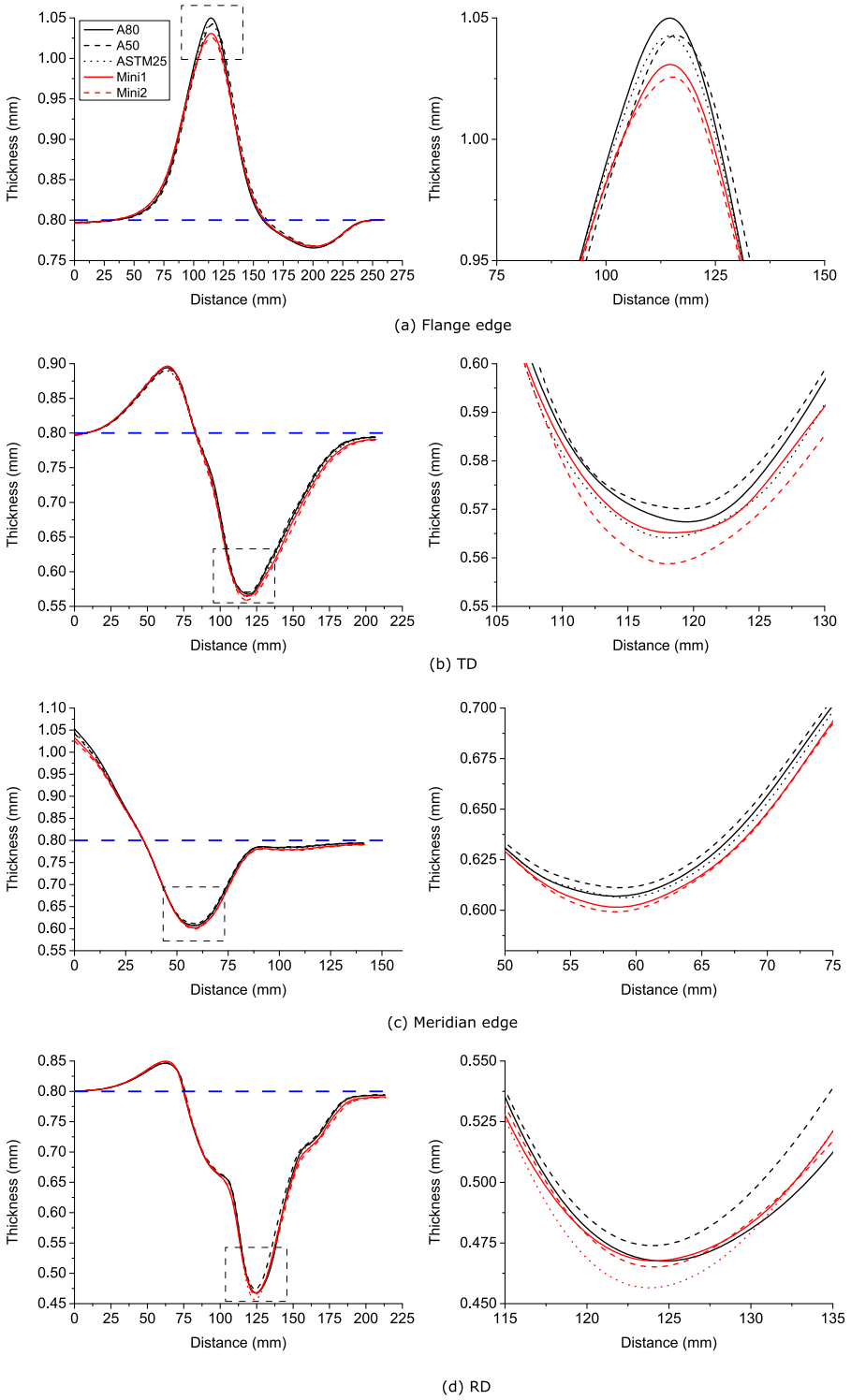

Fig. 12. The thickness (STH) contours on the deformed blank at the end of spring back for different cases. *Right* column shows the enlargement of box region of *Left* column.

greater than 1 for the current simulation set-up (50 mm punch stroke). These locations are primarily located at the ends of the cross-shaped arms, as shown in Fig. 14. The node numbers (the x-axis of Fig. 13) are also labelled which make it easier to link the results of Fig. 13.

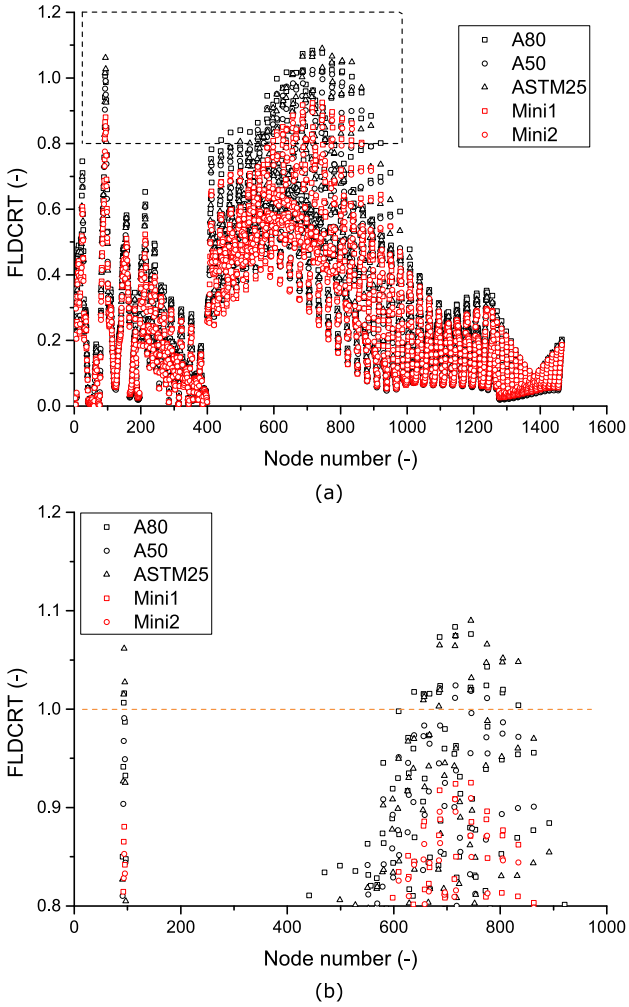

Fig. 13. (a) The damage variable (FLDCRT) value on each node of the deformed blank. The results were obtained at the end of the spring back process. (b) The enlargement of box region in (a).

In terms of the size effect, the results showed that the damage predicted (represented by red data points in Fig. 13) using the results obtained from G-Mini1 and G-Mini2 was smaller compared to the predictions (represented by black data points in Fig. 13) obtained using G-A80, G-A50 and G-ASTM25 results. This indicates that the results obtained from MTS over-predicted (by approximately 15%) the formability of materials as it reports lower damage variable values. One of the main reasons for this is that MTS reports a large strain hardening exponent and requires less punch force for the same value of punch stroke, as discussed in Fig. 10. A relatively low strain hardening material would have better formability. Therefore, care should be taken if MTS is used to predict the formability of materials obtained from RAP.

4.3.4. Forming limit diagram

Fig. 15 shows the forming limit diagrams (points) and curves (Lines) based on results predicted by standard (in black) and non-standard (in red) test-pieces. Firstly, it is worth noting that some points are located above the FLCs (black scatter points above black lines), indicating that failure has occurred on the deformed blank. For instance, Node No. 715, which is located at the ends of the cross arms of the punch, as shown in Fig. 14. However, no red scatter points are above the red curves, indicating that no failure was predicted on the deformed blank. This supports the previous results that suggest that the material predicted by Mini1 and Mini2 has lower rates of work-hardening compared to the material predicted by the standard bars. In terms of the overall scatter point distribution, it is quite similar.

To further investigate the major and minor strains data, k-Means clustering was used. The first step in this analysis is to determine the optimal number of clusters. To do so, the Silhouette scores were calculated, which assess the goodness of clustering and help determine the appropriate number of clusters. The basic principles of k-Means and Silhouette scores were discussed in Section 3.3. Table 6 shows the silhouette scores for different number clusterings. Therefore, a 3-cluster system was selected based on the major-minor strain values on the deformed blank, as it had the highest silhouette score.

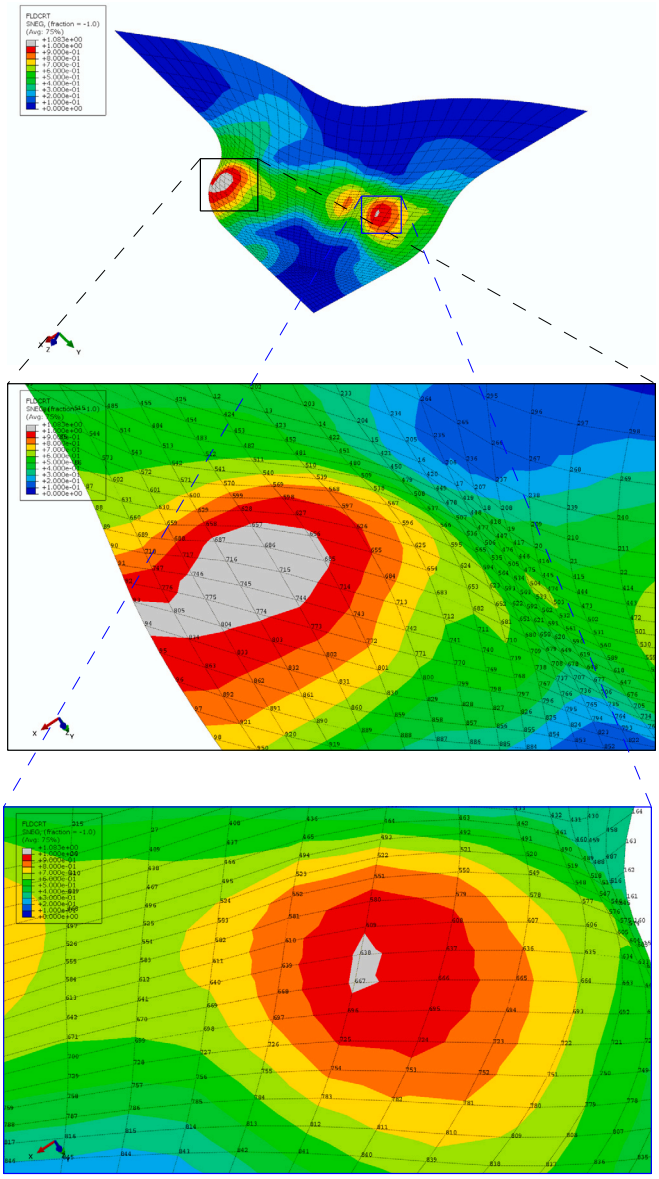

Fig. 14. The damage variable (FLDCRT) contours on the deformed blank at the end of spring back. The node numbers are also presented.

Table 6
The silhouette scores for different number clusterings.

No. of Cluster	2	**3**	4	5	6	7	8	9
Silhouette score	0.489	**0.567**	0.468	0.503	0.531	0.477	0.482	0.487

The forming limit diagrams based on G-A80, G-A50, G-ASTM25, G-Mini1 and G-Mini2 results are shown in Fig. 16. In the figure, C1, C2, and C3 represent Cluster 1, Cluster 2, and Cluster 3, respectively. The regions on the deformed blank represented by the different clusters are shown in Fig. 17. C1 cluster represents the location mostly enduring plain strain conditions, while C2 cluster represents the locations mostly under equibiaxial and biaxial stretching conditions, and C3 cluster represents the locations where deep drawing occurs. Clearly, these regions are very similar for different dimensions. The centroids of each cluster for the five different dimension test-pieces were listed in Table 7. The results showed that the centroids of three clusters for all geometries are close: the standard deviations (Std.) are all in the magnitude of 10^{-3}. This indicates that for the overall predictions of FLD, the non-standard MTS is useable.

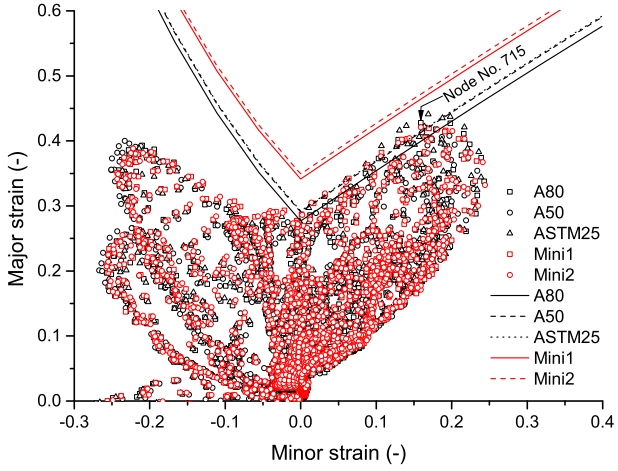

Fig. 15. Forming limit diagrams (points) and curves (Lines) based on results predicted by standard (in black) and non-standard (in red) test-pieces.

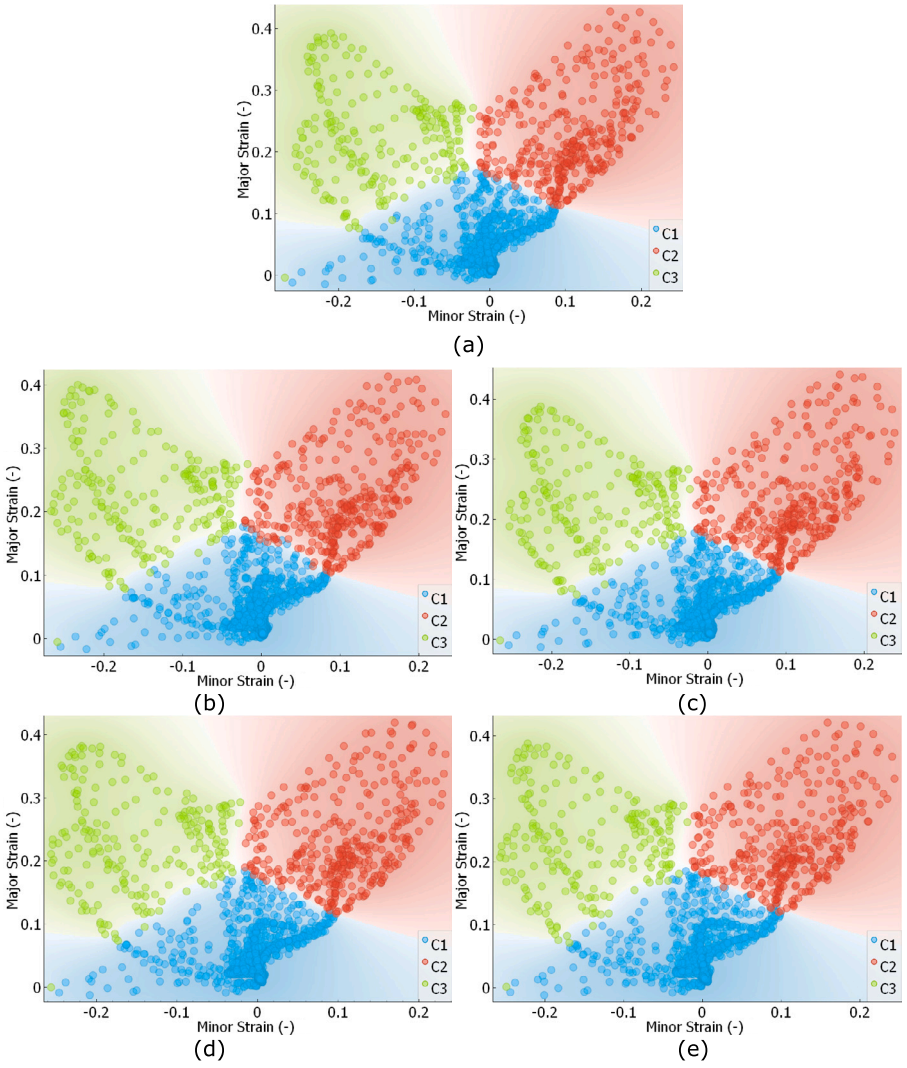

Fig. 16. (a) - (e) Clustered (k-Means) forming limit diagrams based on G-A80, G-A50 G-ASTM25, G-Mini1 and G-Mini2 results, respectively. C1, C2 and C3 denote Cluster 1, Cluster 2 and Cluster 3, respectively.

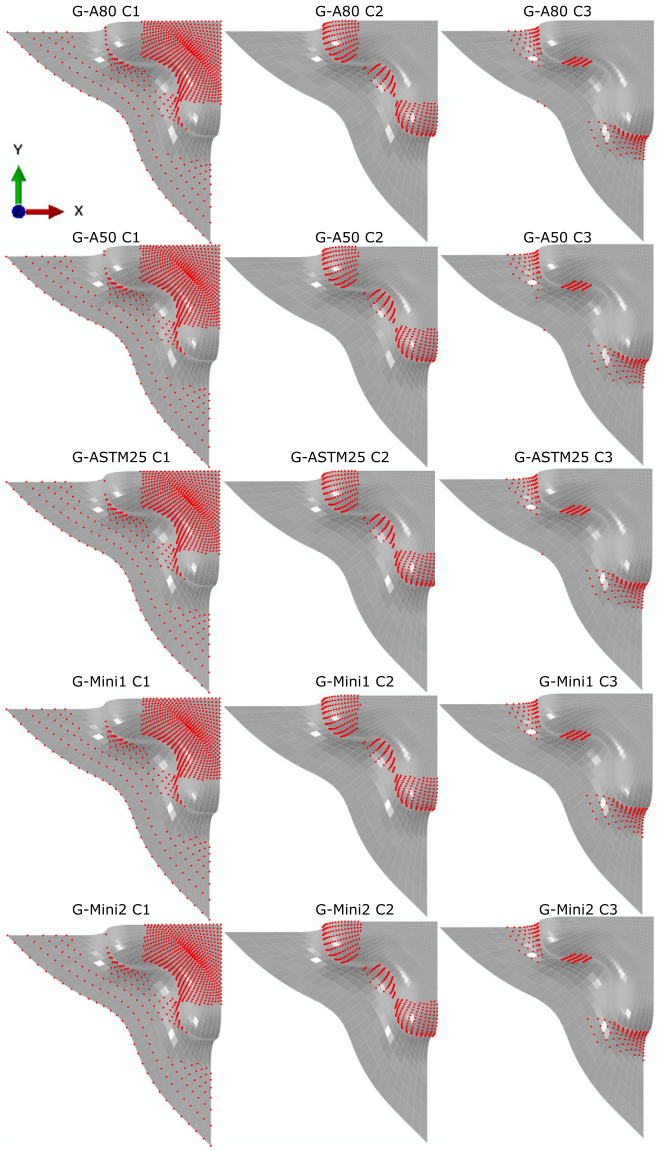

Fig. 17. The clusters (C1, C2 and C3) of nodes on the deformed blank.

Table 7
The major and minor strains' clusters (C1, C2 and C3) centroids comparison for different geometries. The centroids of three clusters for all geometries are close.

Centroid No.	Strain type	A80	A50	ASTM25	Mini1	Mini2	Std.
Centroid 1	Major	0.0495	0.0478	0.0501	0.0523	0.0541	2.45×10^{-3}
	Minor	-0.0079	-0.0085	-0.0078	-0.0073	-0.0066	7.25×10^{-4}
Centroid 2	Major	0.2313	0.2242	0.2336	0.2293	0.2310	3.52×10^{-3}
	Minor	0.1074	0.1030	0.1063	0.1045	0.1057	1.72×10^{-3}
Centroid 3	Major	0.2265	0.2252	0.2284	0.2313	0.2311	2.71×10^{-3}
	Minor	-0.1492	-0.1511	-0.1464	-0.1456	-0.1457	2.43×10^{-3}

5. Further discussion

5.1. Concept to miniaturize tensile specimen

The conventional method to design the miniaturized tensile specimens involves either scaling down dimensions from existing standard measurements or implementing additional modifications following scaling. As the specimen size diminishes, a phenomenon

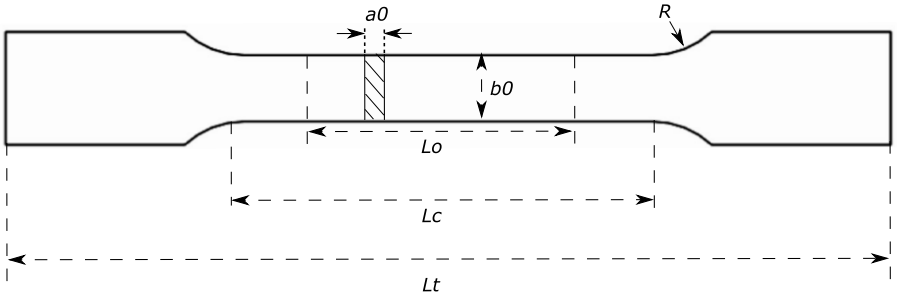

Fig. 18. Definition of L_t, L_c, L_o, a_0, b_0 and R showed in Table 8.

Table 8
Tested tensile bar dimensions. L_t, L_c, L_o, b_0, R and a_0 denote the total length of test piece, parallel length, gauge length, original width of the parallel length of a flat test piece, the shoulder radius and the thickness of the bar, respectively.

	L_t (mm)	L_c (mm)	L_o (mm)	b_0 (mm)	R (-)	L_o/L_c (-)	L_o/b_0 (-)	$(L_c\text{-}2b_0)/L_0$ (-)
A80	260	120	80	20	25	0.67	4	1
A50	200	75	50	12.5	15	0.67	4	1
ASTM25	76	32	25	9	6	0.78	4.17	0.8
Mini1	64	18	12	3	3	0.67	4	1
Modified Mini1	60	12.5	10	3	3	0.8	3.33	0.65
Mini2	51	12	8	2	1.5	0.67	4	1
Modified Mini2	41	9	5	2	1.5	0.56	2.5	1

known as the ‘size effect’ or ‘size dependency’ can play a role. Should the disparities in outcomes between MTS and standard specimens fall within an acceptable range, say, -15% to 15%, it indicates that the MTS results offer a reliable approximation of the mechanical properties. However, if the difference in results exceeds this range, there is still potential utility in using the outcomes, grounded in the fact that MTS can produce consistent, repeatable results. Nevertheless, as specimen thickness is further reduced, potentially reaching around 6 to 10 times the average grain size, the tensile test outcomes of MTS no longer accurately represent the bulk material properties.

For the current work, Mini1 and Mini2 were designed by directly scaling down the parallel length, gauge length, and width of the parallel section from the Standard specimen. However, the relevant ratios among these values remain the same, as shown in Table 8. (Fig. 18 illustrates the definitions of these values on a tensile specimen.). The results of Mini1 and Mini2 perform well.

Further attempts were made to fabricate smaller bars due to constraints posed by the limited materials available through the rapid alloy prototyping process. These efforts yielded Modified Mini1 and Modified Mini2, as illustrated in the table. Notably, the L_0/b_0 ratio for these two dimensions deviates from the standard bars, where it is typically equal to 4. Subsequent tensile tests were conducted, revealing minimal disparities when compared to the results from Mini1 and Mini2 specimens. Consequently, the decision was made to designate the Modified Mini1 and Modified Mini2 as Mini1 and Mini2 for the purposes of this research.

Therefore, we conclude that for the selected steels, the ratio of gauge length to the bar width in the miniaturized tensile specimen does not necessarily need to be 4; a range of 2.5 to 4 is also valid for predicting the materials properties of non-standard bars. The ranges of gauge length to the parallel section length can also be referred to in Table 8.

5.2. Will the designed MTS work for other steels?

In our current exploration of non-standard miniature tensile specimen designs, we undertook testing on four distinct steel variants: dual-phase 800 (DP800) steel, dual-phase 600 (DP600) steel, interstitial-free steel (specifically, DX57, the selected steel for this research), and 3D printed 316L stainless steel. DP800 qualifies as a high-strength low-alloy (HSLA) steel, boasting a tensile strength surpassing 800 MPa. DP600, on the other hand, demonstrates a commendable equilibrium between high strength (exceeding 600 MPa) and formability. The unique attribute of DX57 lies in its interstitial-free composition, characterized by exceedingly low levels of carbon and other interstitial elements. This configuration renders DX57 an exemplary choice for forming applications. Additionally, 3D printed 316L stainless steel was incorporated into the study due to the utilization of additive manufacturing in producing the corresponding tensile bars. This additive manufacturing approach provides an avenue for scrutinizing the non-standard miniature bars via an alternative manufacturing method.

The rationale behind the selection of this diverse array of steels is grounded in our intent to comprehensively assess the performance of the non-standard design across a wider spectrum of steel compositions. Encouragingly, the results from these evaluations indicate that, across all four steel variants, the devised miniaturized tensile specimens exhibit commendable performance in comparison to the standard bars. This encompasses metrics such as yield strength, uniform elongation, ultimate tensile strength, total

elongation, and the r-values. Consequently, these findings suggest that the Mini1 and Mini2 designs could potentially be used for testing the ranges of steel strength and ductility.

6. Conclusions

The work presented in this paper aims to investigate the feasibility of characterizing the formability of interstitial-free steel steels using non-standard miniaturized tensile specimens that can be manufactured using small-scale RAP samples. The study includes both experimental and numerical modelling components. The main conclusions are:

1. The use of miniaturized non-standard tensile test-pieces predicts a larger value of the strain hardening exponent by approximately 18.5%, resulting in an upward shift of the corresponding forming limit curves (predicted by the Keeler Brazier method) on the forming limit diagrams.
2. The stress states for different regions on deformed blank were discussed in detail. Unlike traditional round cup drawing, in addition to the flange, cup wall, and punch region, a new region between the cross punch arms was also investigated.
3. For the same punch stroke, the non-standard miniaturized tensile specimen under-predicted the punch force and the moment when damage appeared, compared to the standard tensile bars. After the blank was deformed, the thickness variation along different paths was compared, and it was found that the maximum difference in thickness values was less than 5%.
4. In terms of the forming limit diagram, the prediction by MTS is very close to the prediction made using the standard test-piece. The overall major-minor strain status of the deformed blank is very similar between the two.

Based on the results obtained from the study, the authors concluded that the miniaturized tensile specimens can be used to predict the formability of IF steels. The numerical simulations were able to accurately predict the forming limit diagrams of the materials, and the results showed that the miniaturized specimens can provide reliable data for characterizing the formability features of IF steels. Overall, the study suggests that the use of miniaturized tensile specimens can provide a cost-effective and efficient method for evaluating the formability of IF steels and other similar alloys manufactured using RAP.

Declaration of competing interest

The authors declare that they have no known competing financial interests or personal relationships that could have appeared to influence the work reported in this paper.

Data availability

Data will be made available on request.

Acknowledgements

The authors would like to thank EPSRC for funding the Rapid Alloy Prototyping Prosperity Partnership project (EP/S005218/1 - ACCELERATING ALLOY DEVELOPMENT THROUGH DELIVERING NOVEL PROTOTYPING SOLUTIONS) which made this work possible. The authors would also like to thank the Welsh Government, European Regional Development Fund (ERDF) and SMART Expertise Wales for funding Materials Advanced Characterisation Centre (MACH1) where the work was carried out. Additionally, the authors would like to thank our reviewers for their work, which contributed to this paper.

References

[1] H. Springer, D. Raabe, Rapid alloy prototyping: compositional and thermo-mechanical high throughput bulk combinatorial design of structural materials based on the example of 30Mn–1.2C–xAl triplex steels, Acta Mater. 60 (12) (2012) 4950–4959.
[2] D. Farrugia, S. Brown, N.P. Lavery, P. Cameron, C. Davis, Rapid alloy prototyping for a range of strip related advanced steel grades, Proc. Manuf. 50 (2020) 784–790.
[3] E.H. Atzema, C.H.L.J.T. Horn, H. Vegter, Influence of tooling layout on sheet forming process analysis, in: European Congress on Computational Methods in Applied Sciences and Engineering, 2004, pp. 1–18.
[4] R.A. Lingbeek, T. Meinders, A. Rietman, Tool and blank interaction in the cross-die forming process, Int. J. Mater. Form. (Suppl) (2008) 161–164.
[5] Banabic, Sheet Metal Forming Processes. Constitutive Modelling and Numerical Simulation, Springer Heidelberg Dordrecht London New York, 2010.
[6] M.S. Niazi, H.H. Wisselink, T. Meinders, J. Huetink, Failure predictions for DP steel cross-die test using anisotropic damage, Int. J. Damage Mech. 21 (2012) 713–753.
[7] A. Ramazani, M. Abbasi, U. Prahl, W. Bleck, Failure analysis of DP600 steel during the cross-die test, Comput. Mater. Sci. 64 (2012) 101–105.
[8] S. Kriechenbauer, R. Mauermann, D. Landgrebe, Deep drawing with local hardening on digital multi-axis servo press, Acta Metall. Sin. (Engl. Lett.) 28 (12) (2015) 1490–1495.
[9] Z. Deng, R. Hennig, Influence of material modeling on simulation accuracy of aluminum stampings, IOP Conf. Ser.: J. Phys. Conf. Ser. 896 (2017) 012025.
[10] N. Habibi, V. Sundararaghavan, U. Prahl, A. Ramazani, Experimental and numerical investigations into the failure mechanisms of TRIP700 steel sheets, Metals 8 (2018) 1073.
[11] N. Habibi, A. Ramazani, V. Sundararaghavan, U. Prahl, Failure predictions of DP600 steel sheets using various uncoupled fracture criteria, Eng. Fract. Mech. 8 (2018) 367–381.
[12] P. Muller, S. Kriechenbauer, W. Drossel, Experimental analysis of the elastic boundary conditions of press machines for modelling the deep-drawing process, Int. J. Adv. Manuf. Technol. 101 (2019) 579–592.

[13] A. Nakwattanaset, S. Suranuntchai, S. Panich, Strain- and stress-based forming limit curves of DP440 steel sheet with application to the cross-die forming test, AIP Conf. Proc. 2279 (2020) 050004.
[14] S. Kriechenbauera, P. Muller, R. Mauermanna, W. Drossel, Evolutionary optimization of deep-drawing processes on servo screw presses with freely programmable force and motion functions, Proc. CIRP 104 (2021) 1482–1487.
[15] L. Zhang, W. Harrison, M.A. Yar, S.G.R. Brown, N.P. Lavery, The development of miniature tensile specimens with non-standard aspect and slimness ratios for rapid alloy prototyping processes, J. Mater. Res. Technol. 15 (2021) 1830–1843.
[16] L. Zhang, W. Harrison, S. Mehraban, S.G.R. Brown, N.P. Lavery, Size effect on the post-necking behaviour of dual-phase 800 steel: modelling and experiment, Materials 16 (2023) 1458.
[17] L. Zhang, W. Harrison, M.A. Yar, S. Mehraban, S.G.B. Brown, N.P. Lavery, Use of miniaturized tensile specimens to evaluate the ductility and formability of dual phased steels for Rapid Alloy Prototyping, Mater. Sci. Eng. A 875 (2023) 145075.
[18] BSI British Standards, Metallic Materials—Tensile Testing Part 1: Method of Test at Ambient Temperature, BSI British Standards, London, UK, 2009.
[19] A.S.T.M. International, Standard Test Methods for Tension Testing of Metallic Materials, ASTM International, West Conshohocken, PA, USA, 2013.
[20] J.H. Hollomon, Tensile deformation, Trans. Metall. Soc. AIME 162 (1945) 268–290.
[21] J.L. Ferreira, L.P. Moreira, M.C. Cardoso, Analysis of the pre-straining effects on the limit strains of interstitial-free steel: experiments and elasto-plastic modeling of strain and stress-based forming limit curves 43 (2021) 82.
[22] S.P. Keeler, W.G. Brazier, Relationship between laboratory material characterization and press-shop formability, in: Proc. Conf. on Microalloy, vol. 75, 1977, pp. 517–528.
[23] K. Chen, A.J. Carter, Y.P. Korkolis, Flange wrinkling in deep-drawing: experiments, simulations and a reduced-order model, J. Manuf. Mater. Process. 6 (2022) 76.
[24] K. Bouchaâla, M.F. Ghanameh, M. Faqir, M. Mada, E. Essadiqi, Evaluation of the effect of contact and friction on deep drawing formability analysis for lightweight aluminium lithium alloy using cylindrical cup, Proc. Manuf. 46 (2020) 623–629.
[25] J. Wu, R. Balendra, Y. Qin, A study on the forming limits of the hydro-mechanical deep drawing of components with stepped geometries, J. Mater. Process. Technol. 145 (2004) 242–246.
[26] C. Robert, A. Delameziere, P.D. Santo, J.L. Batoz, Comparison between incremental deformation theory and flow rule to simulate SheetMetal forming processes, J. Mater. Process. Technol. 212 (2012) 1123–1131.
[27] F. Ayari, T. Lazghab, E. Bayraktar, Parametric finite element analysis of square cup deep drawing, Arch. Comput. Mater. Sci. Surf. Eng. 1 (2) (2009) 106–111.
[28] A. Wifi, A. Mosallam, Some aspects of blank-holder force schemes in deep drawing process, J. Achiev. Mater. Manuf. Eng. 24 (1) (2007) 315–323.
[29] H. Tschaetsch, Metal Forming Practise Processes – Machines – Tools, Originally German edition published by Vieweg Verlag, Wiesbaden, 2005.